Complementary use of x-ray dark-field and attenuation computed tomography in quantifying pulmonary fibrosis in a mouse model

Nelson, Brandon, Leng, Shuai, Koenig, Thomas, McCollough, Cynthia

Brandon J. Nelson, Shuai Leng, Thomas Koenig, Cynthia H. McCollough, "Complementary use of x-ray dark-field and attenuation computed tomography in quantifying pulmonary fibrosis in a mouse model," Proc. SPIE 12036, Medical Imaging 2022: Biomedical Applications in Molecular, Structural, and Functional Imaging, 120360W (4 April 2022); doi: 10.1117/12.2612877

Event: SPIE Medical Imaging, 2022, San Diego, California, United States

Complementary use of x-ray dark-field and attenuation computed tomography in quantifying pulmonary fibrosis in a mouse model

Brandon J. Nelson*[a,b], Shuai Leng[a,b], Thomas Koenig[b,c], Cynthia H. McCollough[a,b]
Department of Radiology, Mayo Clinic, Rochester, MN 55905; [b]Graduate Program in Biomedical Engineering and Physiology, Mayo Clinic Graduate School of Biomedical Sciences, Rochester, MN 55905; [c]Ziehm Imaging, Lina-Ammon-Str. 10, 90471 Nuremberg, Germany

ABSTRACT

X-ray dark-field measured on laboratory sources with large focal spots and detector apertures is sensitive to intra-pixel phase gradients abundant in the lungs due to its hierarchical structure of subdividing airways terminating in thin-walled alveoli. This work leverages this sensitivity to exploit complementary information from x-ray dark-field and attenuation computed tomography (CT) images to improve quantification of morphology in pulmonary fibrosis. Specifically, a dark-field enhanced attenuation technique is developed to restore edges and small features in the attenuation image lost to blurring by appropriately scaling and subtracting the dark-field image. An intratracheally treated bleomycin mouse model of pulmonary fibrosis was used to evaluate the impact of the proposed dark-field enhanced attenuation technique on quantifying fibrosis extent. The mouse model was fixated *ex vivo* to be imaged with a Talbot-Lau grating interferometer micro-CT to generate x-ray dark field and attenuation volumes of 60 µm voxels. Then the specimen was imaged with a reference micro-CT scanner at 5 µm voxel resolution to get a ground truth approximation of local structure. The volumes were co-registered for visual and pixelwise comparisons. Qualitative image comparisons were used to assess visual sharpness while Bland-Altman plots were used to assess agreement with the reference scan at quantifying fibrosis in terms of tissue area fraction measured in 80 randomly sampled nonoverlapping 2 mm square patches. Visual comparisons demonstrated enhanced sharpness and retention of small lung structures while Bland-Altman analysis revealed an improved agreement ratio of 0.544 compared to 0.374 in the original attenuation image with a reduction in variance. These results demonstrate that dark-field and attenuation images can be used together to improve resolution of small structures and aid in quantification of pulmonary fibrosis in a mouse model.

Keywords: dark field, pulmonary fibrosis, bleomycin, computed tomography

1. INTRODUCTION

Computed tomography (CT) is the primary tool to diagnose and quantify the extent and severity of pulmonary fibrosis which is characterized by a thickening of the lung interstitium and displacement of airspace with fibrotic tissue[1]. Sensitivity to early-stage fibrosis is often resolution limited as increases in the interstitium can be offset by increases in airspace volume leaving volume density largely unchanged. Additionally, density changes alone are not specific enough for a radiographic or CT diagnosis, rather a characteristic disease pattern must be thoroughly developed and identifiable resulting in confident diagnoses only in advanced disease stages[2]. Micro-CT studies have shown that fibrosis severity and extent are better estimated with higher resolution scans[3,4]. These findings have been further supported in full scale CT scanners with the introduction of photon counting detectors capable of higher resolution imaging with greater geometric efficiency[5,6]. X-ray dark-field is an alternative approach to measuring small structures with existing sources and detectors using Talbot-Lau grating interferometry[7]. X-ray dark-field is more sensitive in detecting structural changes otherwise too small to be resolved on the same detector via traditional absorption radiography and has been shown to be more sensitive at detecting various lung pathologies in both small and large animal pilot studies including emphysema[8–10], inflammation[11,12], lung cancer[13], and fibrosis[14].

While originally introduced as deriving from small-angle x-ray scattering[7], an energy dependent material property related to both composition and structure size[15], x-ray dark-field from laboratory-based systems with large focal spots and detector pixels is now better understood as arising from intra-pixel phase gradients[16]. Like how x-ray attenuation measurements are relative to the applied x-ray energy, dark-field measurements are also relative to the spatial resolution of the system amongst other sources including beam hardening[17,18]. This spatial resolution dependence is more pronounced with *in vivo* studies where dose and scan time requirements dictate the use of larger detectors and source

Medical Imaging 2022: Biomedical Applications in Molecular, Structural, and Functional Imaging,
edited by Barjor S. Gimi, Andrzej Krol, Proc. of SPIE Vol. 12036, 120360W
© 2022 SPIE · 1605-7422 · doi: 10.1117/12.2612877

sizes covering tens of source and analyzer periods. While the intra-pixel phase gradient interpretation of x-ray dark-field is useful in explaining dark-field's sensitivity to sharp edges[19] and second order phase gradients[20], it exposes challenges to the quantitative use of dark-field as its signal can be altered by processes affecting spatial resolution including detector pixel size, focal spot size, and magnification[16]. In x-ray attenuation imaging insufficient spatial resolution is responsible for partial volume averaging where tissues of differing absorption contained within a voxel are averaged together. In lung imaging this results in blurred boundaries between solid tissues and is responsible for the wide range of lung HUs in the parenchyma due to inflation volume and pathology[1]. This further limits the application of conventional absorption based CT images in detection and quantification of early stage lung fibrosis. The purpose of this work is to introduce and validate a means of leveraging dark-field's intra-pixel phase gradient sensitivity with the simultaneously acquired attenuation signal to both improve spatial resolution and contrast within the lung parenchyma in the attenuation image. These combined effects are of practical benefit in interpreting and quantifying the extent of pulmonary fibrosis demonstrated in this work via grating interferometer CT imaging (yielding attenuation, phase, and dark-field image contrasts of the lung simultaneously) of a fixed *ex vivo* mouse model of pulmonary fibrosis.

2. METHODS AND MATERIALS

2.1 General approach to dark-field enhanced attenuation

To leverage the unresolvable edge information of x-ray dark-field to improve image quality first assume that dark-field D is entirely derived from intra-pixel phase gradients, defined here as the difference between the true phase distribution $\Phi(x)$ and its blurred measurement $\Phi'(x)$:

$$D(x) = \Phi'(x) - \Phi(x). \tag{1}$$

Thus, in an experimental measurement where only the measured dark-field D and phase Φ' are available the true unblurred phase distribution $\Phi(x)$ could be estimated by rearranging eq (1) as:

$$\Phi(x) = \Phi'(x) - D(x). \tag{2}$$

In practice however, rather than measuring phase $\Phi(x)$, grating interferometers measure the differential phase contrast $\partial\Phi'/\partial x$, where x is in the phase stepping direction, perpendicular to the grating rule. While differential phase can be integrated in the phase step direction to recover $\Phi(x)$, noise from the detectors, photon statistics, and phase step vibrations become integrated yielding low-frequency noise effects[21–23]. While iterative methods have been introduced to recover this phase information it remains a non-trivial task[24,25]. Furthermore, in the context of lung imaging phase is a circular measurement $(-\pi, \pi)$ and phase wrap also remains a challenging task due to the abundance of air-tissue interfaces[26,27].

Meanwhile, x-ray attenuation is already well established in measuring lung structure due to the natural high contrast between air and tissue[1]. However due to spatial resolution limitations of attenuation imaging, partial volume effects result in blurring, reducing the sensitivity of attenuation radiography and CT to detect small pulmonary nodules[28] and quantify fibrosis extent[3]. Given that attenuation and phase coefficients are correlated at medical energies[29] $A = \alpha\Phi$, dark-field can also be used to estimate edges lost from partial volume averaging in measured attenuation images $A'(x)$, a process hereafter referred to as dark-field enhanced attenuation (DFEA) to better estimate the true attenuation distribution:

$$\mathrm{DFEA}(x) = A'(x) - \alpha D(x). \tag{4}$$

When imaging biological tissues based on the assumption that for a constant energy and similar materials the attenuation and phase coefficients are approximately proportional the scalar $\alpha = \mu_{water}/\Phi_{water}$. Assuming this ratio does not vary substantially between most biological materials it could be estimated using a water calibration scan.

2.2 Sample preparation

To assess the impact of dark-field enhanced attenuation on quantifying pulmonary fibrosis a bleomycin mouse model of pulmonary fibrosis was used. All animal studies were approved by Mayo Clinic's Institutional Animal Care and Use Committee. Bleomycin was administered intratracheally and incubated for 21 days before excising the lungs ex vivo[30]. To get a ground truth measure of lung structure, the lungs were fixated in an inflated state *ex vivo* to enable reproducible high-resolution imaging to compare against our experimental measurements.[31]A fixative solution of 50% PEG 400, 25%

Ethyl alcohol, 10% formaldehyde and 15% water was then administered via the trachea to a filling pressure of 20 cm water column and immersed in the same solution for seven days before being air inflated at 25 mmHg and dried for 72 hours[32]. This fixation method preserves native air-tissue contrast as well as the inflated structure of the lung, and is a standard method for *ex vivo* structural imaging as determined by the American Thoracic Society guide on structural lung imaging[33].

2.3 Image acquisition

Experimental attenuation and dark-field images used in this study were generated with a Talbot-Lau grating interferometer incorporated into a tabletop micro-CT system, summarized in Figure 1. The interferometer geometry had a design energy of 40 keV operated at the first Talbot order. Three grating optics were used including a source absorption grating (G_0), a $\pi/2$ phase shift grating (G_1), and an analyzer absorption grating (G_2) with periods 10, 2.4, and 4.8 μm respectively. These gratings were positioned with a G_0-G_1 distance of d_{01}=522 mm and G1-G2 distance of d_{12}=251 mm. Further grating details are summarized in Table 1. Phase step curves were acquired by mechanically translating G_2 six equidistant steps covering one Talbot carpet period with an exposure time of 1.5 seconds per step and mean visibility of 14.7% in a flatfield acquisition. The source was a PANalytical XRD C-tech model with 400 μm x 800 μm focal spot size operated at 55 kVp and 35 mA filtered with a 0.2 mm beryllium window. The detector was a Princeton Instruments Pixis 2048F CMOS detector, binned four by four to yield 52 μm square pixels. Dark field and attenuation contrast projections were acquired over 360 degrees at 0.25 degree increment, retrieved using the Fourier method[34] and reconstructed into volumes of 60 μm cubic voxels following Ram-Lak filtering using the FDK method implemented in the TIGRE reconstruction suite[35].

2.4 Disease quantification and statistical evaluation

In this study the extent of pulmonary fibrosis was quantified in terms of tissue area fraction measured in local regions of axial image slices. Tissue area fraction is defined as the fraction of pixels in a local patch containing tissue over the total patch area after excluding major anatomic structures of the lung such as major bronchi, large blood vessels, the heart, and esophagus. This quantity includes small airway walls, small blood vessels, and fibrotic loci. It has a value of 5-10% in healthy parenchyma and increases progressively with fibrosis severity[3,36]. This local patch-based analysis is able to account for the heterogenous distribution of fibrosis found in the bleomycin mouse model.

As sensed by x-rays, the lungs are approximately composed of two main materials, tissue with attenuation properties like water, and the air trapped inside. Due to partial volume averaging voxels containing both materials will measure the average weighted by the relative abundance of each contained within the voxel. This accounts for the broadened range in attenuation coefficients measured in the lungs due to regional differences in inflation and density affecting tissue fraction measurements. As a result, an imaging system with higher resolution is less susceptible to partial volume effects and can better separate tissue spaces from air spaces in the lungs which are composed of many small and high frequency interfaces of air and tissue. For this reason, following CT acquisition on the grating interferometer, the lung specimen was subsequently imaged on a reference Bruker 1276 micro-CT system to acquire a high-resolution volume of the specimen at 5 μm isotropic voxels to get a “ground truth” approximation of the lung structural properties. The reference scan was acquired at 40 kVp, 120 μA with a four frame average of 0.75 s exposure per projection over 360 degrees with a 0.15 degree increment and reconstructed into 5 μm voxels using the provided Bruker NR Recon package This reference dataset was registered to the grating interferometer derived attenuation contrast CT volume using the Expert Automated Registration module in 3D Slicer[37].

From the co-registered 60 μm voxel interferometer CT and 5 μm voxel reference micro-CT images, 2 mm square nonoverlapping patches were selected in a process of uniform random sampling[36] where 10 slices were randomly selected from the CT volume with eight patches randomly selected per slice. Slices overlapping the heart, esophagus, major bronchi, and major blood vessels were excluded and did not contribute to the patch count. Tissue fraction in each patch was measured with ImageJ[38] using a global intensity threshold, selected automatically using minimum error thresholding[39] applied to the whole volume intensity histogram for each image series.

The impact of dark-field enhanced attenuation on fibrosis quantification (tissue area fraction) was assessed in terms agreement with the 5 μm reference micro-CT scan. This agreement was quantified in terms of Bland-Altman plots of the ratio of the measured tissue area fraction to the reference measurement and plotted against the mean value from both measures[40]. These plots were also generated with the original attenuation images to assess impact of incorporating dark-field information.

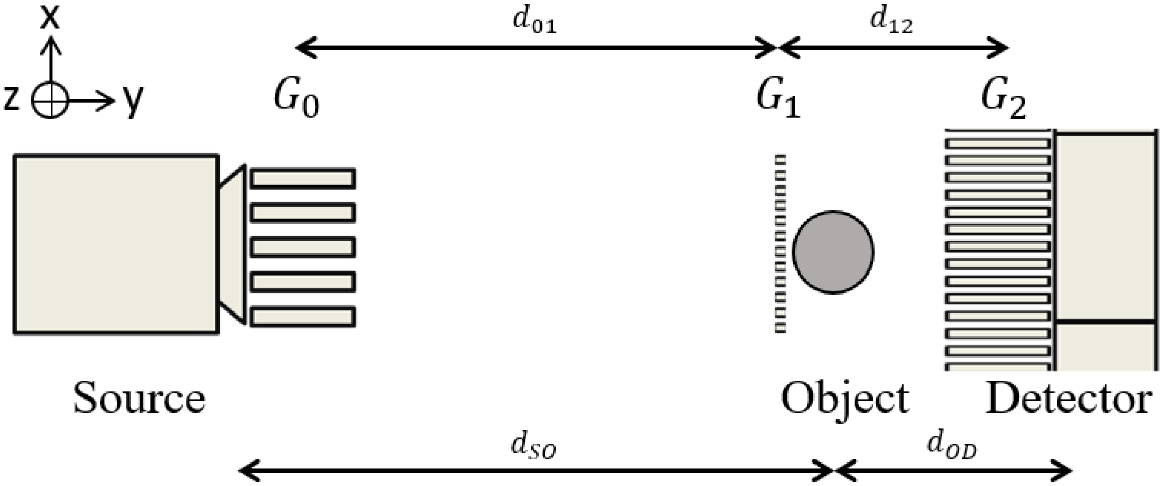

Figure 1. Diagram of the Talbot-Lau grating interferometer used in this study. The source grating G_0 spatially modulates x rays from a source with a large focal spot. The phase shift grating G_1 produces a downstream Talbot carpet sensitive to phase shifts induced by the object in the beam path. G_2 matches the period of the Talbot interference pattern at its location to the sample the high frequency interference pattern by translating G_1 or G_2 in the x direction. Distances d between gratings are noted at the top with distances between the source, object, and detector shown below.

Table 1. Grating specifications of the experimental Talbot-Lau system.

Grating	Period (μm)	Duty cycle (%)	Lamellae material	Lamellae height (μm)	Size (cm^2)	Substrate material	Substrate thickness (μm)
G_0	10.0	55	Au	120	6 x 6	graphite	500
G_1	3.24	55	Au	2.6	6 x 6	Si	200
G_2	4.8	55	Au	120	6 x 6	graphite	500

3. RESULTS

A qualitative comparison of the original attenuation and dark-field images acquired from the grating interferometer CT scan of the fixed lung along with their combined images are shown in Figure 2. In the original attenuation image (Fig. 2a) large structures like the esophagus, major bronchi, and large blood vessels are resolvable. However, smaller vessels and airways in the lung parenchyma are blurred out yielding a textured pattern rather than clearly resolvable features. The simultaneously acquired dark-field image (Fig. 2b) reveals edge enhancements in the parenchyma exposing these smaller structures as well as highlighting the boundaries around larger structures. In the dark-field enhanced attenuation image (Fig. 2c) the dark-field image is scaled and subtracted from the attenuation according to Eq. 4, yielding a qualitative improvement in resolving smaller structures blurred out in Fig. 2a. In particular, the honeycombing fibrosis pattern is more apparent following enhancement of the attenuation image with dark-field edge information (red arrow in Fig. 2c). Such patterns are important in distinguishing fibrosis from other hyperattenuating pathology such as infiltration. Further edge enhancement is also possible by increasing the relative contribution of dark-field beyond the α value measured from water calibration (Fig. 2d).

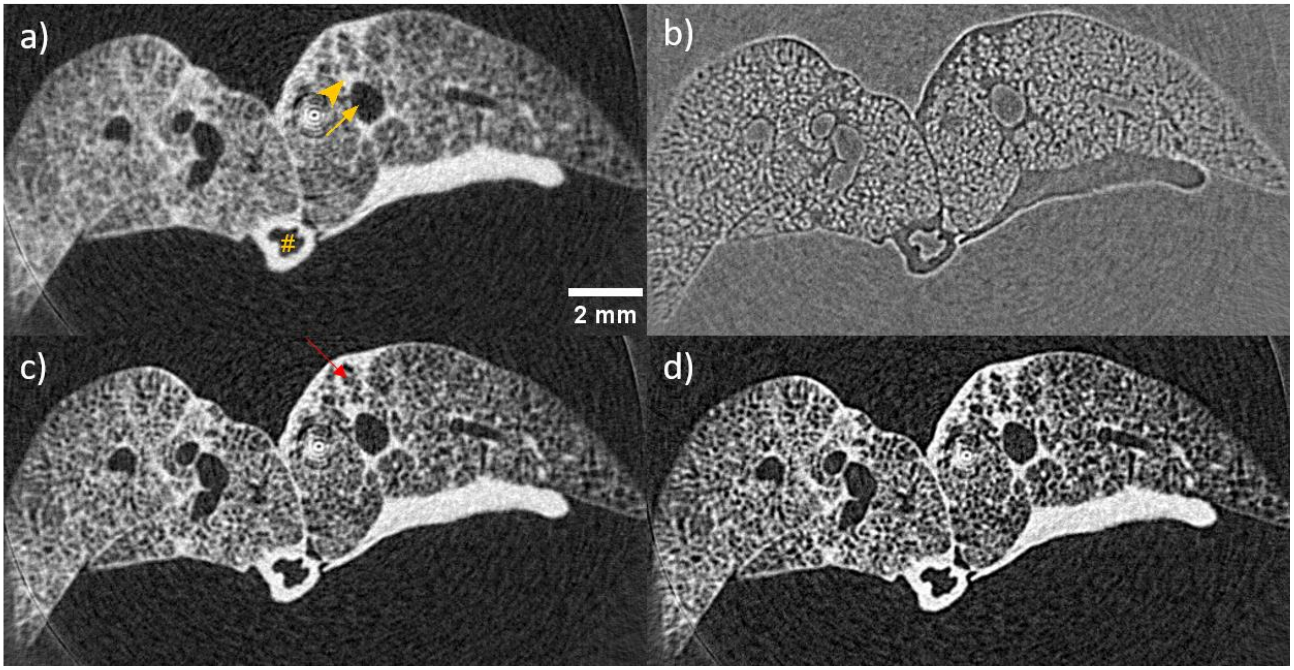

Figure 2. Laboratory-based x-ray dark-field acquired with large detector pixels corresponds to intra-pixel phase gradients enhancing edges and contrast of the lung parenchyma composed of sequentially smaller airways, blood vessels, and gas exchanging alveolar walls. The correlation between attenuation and phase coefficients enables complementary use of dark-field to restore edges and enhance parenchyma contrast. a) Original interferometer attenuation image. Examples of specific anatomy include the esophagus (#), blood vessels (orange arrowhead), and major bronchus (orange arrow). b) original interferometer dark-field image. c) dark field enhanced attenuation image (DFEA) where the dark-field image (b) is subtracted from the attenuation image (a) after first being scaled by factor $\alpha = 0.022$, the measured ratio of water attenuation and phase coefficients. The result is visually sharper with more small airways and blood vessels resolvable than in the original attenuation image (a). The red arrow highlights an example of honeycombing in a fibrotic locus made more conspicuous in the combined image. d) increasing this scalar value to $\alpha = 0.1$ results in a further edge-enhancing effect and further parenchyma contrast enhancement. Image subsets a), c), and d) are all shown at the same display settings of min/max: 0/0.03 mm^{-1}, while the dark-field image is shown with display setting min/max: -0.1/0.1.

In addition to restoring small features and edges lost to blurring, dark-field enhanced attenuation also increases contrast of large structures like blood vessels and fibrosis. This is due to the abundance of unresolvable features in the lung parenchyma giving an overall positive signal in the dark-field image, while homogenous voxels covering resolvable blood vessels or fibrosis have mean zero signal. Looking at the distribution of voxels (Figure 3) following subtraction in dark-field enhanced attenuation, voxels in the parenchyma get shifted to lower values closer to the air while the restoration of small features and edges yields a small increase in the height of the tissue peak.

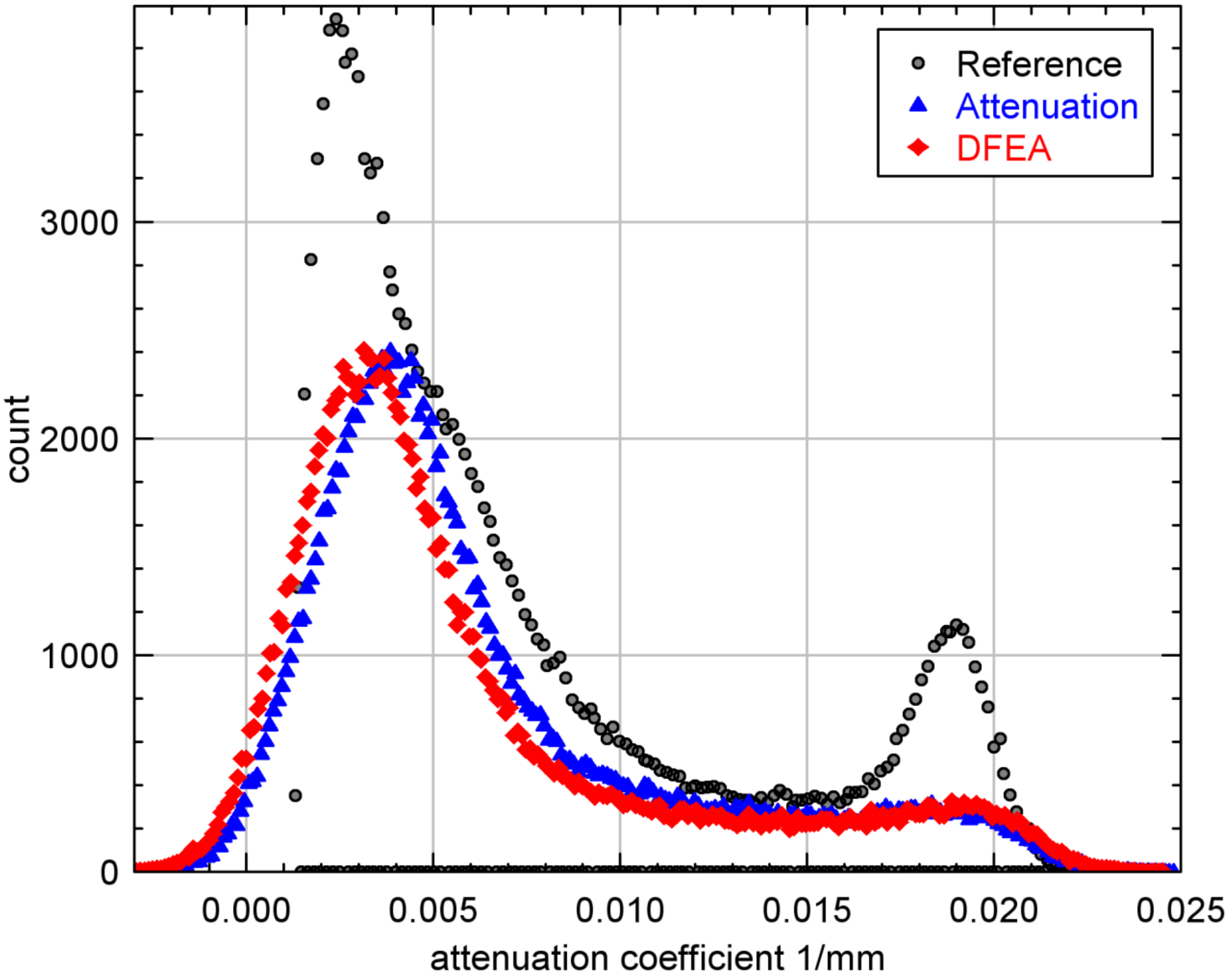

Figure 3. Subtracting scaled dark-field from attenuation in dark-field enhanced attenuation (DFEA) yields greater histogram separation of air (left peak) and soft tissue (right peak) more closely resembling the distribution acquired from a 5 µm voxel high-resolution reference micro-CT scan.

The impact of this increased histogram separation on fibrosis was evaluated by comparing intensity-based tissue segmentations to measure tissue area fraction, a quantity related to fibrosis progression. Figure 4 shows a representative patch comparing segmentations from the original attenuation, the dark-field enhanced attenuation image, and the co-registered 5 µm reference micro-CT image. Compared to the original attenuation image the dark-field enhanced image has more small features retained in the segmentation which are visually consistent with the reference scan image.

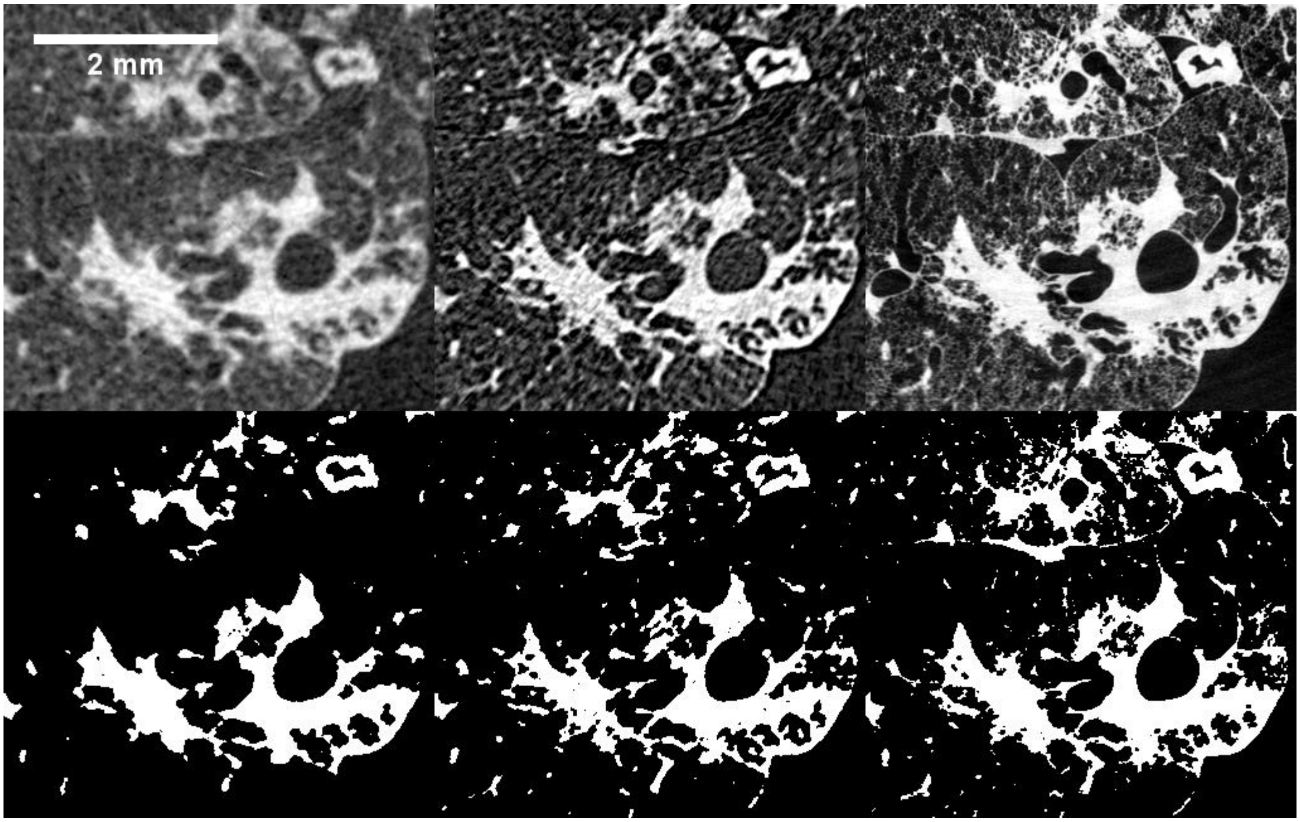

Figure 4. Comparison of intensity-based threshold segmentation between attenuation (left) and dark-field enhanced attenuation (center) against co-registered reference 5 µm voxel micro-CT (right). Top: Representative image patches of all three images are shown at the same display settings, min/max: 0/0.03 mm^{-1}. In this patch reticular fibrosis and honeycombing is present around the large airways. Bottom: Threshold-based intensity segmentations with thresholds determined automatically via minimum error thresholding applied to the whole volume histogram.

To assess agreement with the 5 µm reference scan all 80 patches were segmented using an intensity threshold determined automatically via minimum error thresholding from the global histogram of each image series. From these segmentations tissue area fraction was measured and presented as a Bland-Altman plot (Figure 5) where the ratio with the reference measure for each patch is plotted against the mean tissue fraction between both measurements[40]. Using the ratio rather than the absolute difference accounted for a negative proportionality observed in both experimental measurements. This observation was due to the reticular nature of fibrosis and presence of honeycombing in large fibrotic loci of the mouse model (Figure 4) where small spindly structures are in greater abundance in higher tissue fraction patches and lost in the segmentation. This transformation corrects for this proportionality and better demonstrates agreement in lower tissue fraction patches more representative of early-stage fibrotic loci. From this we observed an improved agreement ratio in the dark-field enhanced attenuation (DFEA) images from 0.374 to 0.544 along with a reduction in the 95% limits of agreement describing the measurement spread (summarized in Table 2). At higher tissue fractions we observed the agreement of DFEA to approach that of the original attenuation image as the relative influence of restoring small features and edges is less pronounced when fibrotic loci become larger and more solid masses. On the other hand, at lower tissue fractions, more representative of early fibrosis, DFEA images show much improvement over original attenuation images in terms of agreement with reference standard. Both techniques show underestimation of tissue fraction compared to reference standard acquired with 5 µm resolution. However, original attenuation images show significant dependence on tissue fraction. A clear trend of increased underestimation toward low tissue fractions. On the other hand, DFEA shows much less dependence on tissue fraction, with more consistent underestimation (bias). This bias can be corrected (subtracted) using calibration in practice. These results demonstrate improved agreement with the reference 5 µm scan by incorporating dark-field information containing unresolved edge information into attenuation images acquired on a lower resolution 60 µm interferometer scan.

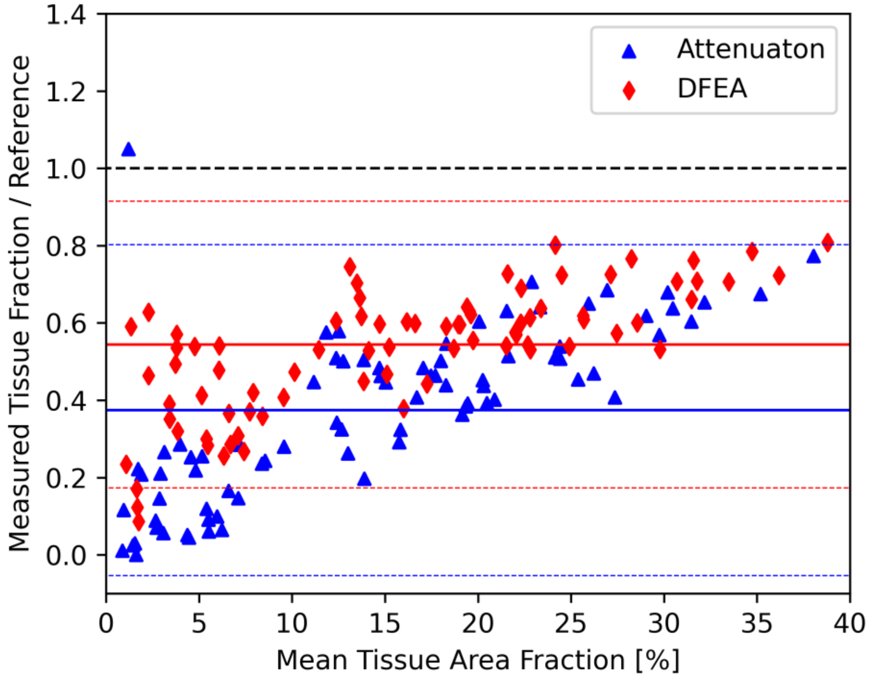

Figure 5. Bland-Altman plot of tissue area fractions measured on a low resolution 60 µm voxel grating interferometer CT system compared to an approximate ground truth high resolution 5 µm voxel reference micro-CT. The contribution of dark-field enhanced attenuation (DFEA) with greater contribution of dark-field information to improve segmentation accuracy in terms of closeness to the reference scan is shown. The thick dashed black line shows an ideal measurement with no bias from the reference measure for an agreement ratio of 1. Red and blue solid lines correspond to the mean agreement ratios, while the corresponding thin dashed lines are the 95% limits of agreement calculated as ±1.96 times the standard deviation of the ratios[40].

Table 2. Summary of Bland-Altman results plotted in Figure 4. The agreement ratio is defined as the measured tissue area fraction divided by the reference measurement and the 95% limits of agreement correspond to 1.96 times the standard deviation of the agreement ratios from the measured patches.

Series	Agreement ratio	95% limits of agreement
Attenuation	0.374	0.428
DFEA	0.544	0.370

4. DISCUSSION

High resolution micro-CT is capable of quantifying pulmonary fibrosis extent with greater accuracy and precision than histology or biochemical assays[3]. However, the requirements of long scan times due to x-ray source output limitations and small fields of view due to detector size restrictions limits its applicability to *ex vivo* organ imaging. Meanwhile, the feasibility of x-ray dark-field for *in vivo* whole body CT imaging has already been demonstrated[41,42]. While the quantitative value of using dark-field alone when measured on laboratory-based grating interferometers is limited due to its spatial resolution sensitivity[16], in this work we presented a means of leveraging dark-field to enhance sharpness and contrast of attenuation images. This method is based on the assumptions of dark-field primarily deriving from intra-pixel phase gradients and on the proportionality between attenuation and phase coefficients in biological tissues at relevant x-ray energies. Using a bleomycin mouse model of pulmonary fibrosis, we showed that this dark-field enhanced attenuation technique was able to restore edges and small features while increasing parenchyma contrast. By using a fixated ex vivo lung we were able to reproducibly scan the same specimen to get a ground truth approximation of the lung structure using a high-resolution reference micro-CT to confirm the restoration of small features. Performance in quantifying fibrosis was evaluated against the original interferometer attenuation images in terms of agreement with the reference scan in tissue area fraction measured in 80 randomly sample patches from the lung. Using Bland-Altman plot analysis we found that incorporating the dark-field edge information improved agreement with the high-resolution reference scan in terms of reduced bias and a reduction in spread due to the increased histogram separation between the air and tissue voxel peaks. Determining the acceptable limits of agreement are application specific and are beyond the scope of this work but use of image denoising is one potential means of further decreasing these limits of agreement.

The limitations of this study include the limited sample size and potential registration errors of the reference scan with the interferometer data. During the fixation process some samples did not fully inflate while air-drying and were excluded from the study. Errors in the registration arose from rescanning the lungs on a different scanner where small deformations could have occurred in the mounting process. While registration was performed automatically and was validated by visual inspection some errors could be present that could account for additional sources of bias when assessing agreement. However, this bias is equivalent for both experimental scans being compared as they derive from the same raw data. Future work remains to increase the sample size by imaging more lung samples and further validate the method with task independent image quality assessment.

Previous works have largely focused on the use of dark-field alone for the detection of lung diseases[8,10,14,43]. However, some studies have leveraged the attenuation information simultaneously acquired in grating interferometer scans, notably normalized scatter where the penetration depth dependence of dark-field radiographs is removed via pixel-wise division with the attenuation image[9,44,45]. This work differs by focusing on how dark-field's correlation with sharp edges and phase gradients in the lung can be used to improve the sharpness and parenchyma contrast in the attenuation image, improving the conspicuity and segmentation performance of small structures with existing detectors and sources.

5. CONCLUSIONS

Intra-pixel phase gradients are the predominant source of dark-field signal in laboratory-based x-ray grating interferometers. Here we have shown how this gradient information in dark-field images can be used to restore spatial resolution and enhance contrast between homogenous and heterogenous structures by subtracting it from the attenuation image. An ex-vivo mouse lung model of pulmonary fibrosis was used to demonstrate the ability of this new technique, dark-field enhanced attenuation (DFEA), at improving resolution of small structures and enhancing parenchymal contrast. Improved performance at quantifying fibrosis was demonstrated in terms of improved agreement with a high-resolution reference micro-CT scan.

REFERENCES

[1] M. Mascalchi, G. Camiciottoli, and S. Diciotti, "Lung densitometry: why, how and when," J. Thorac. Dis. **9**(9), AME Publishing Company (2017) [doi:10.21037/jtd.2017.08.17].

[2] F. J. Martinez et al., "Idiopathic pulmonary fibrosis," 1, Nat. Rev. Dis. Primer **3**(1), 1–19, Nature Publishing Group (2017) [doi:10.1038/nrdp.2017.74].

[3] C. J. Scotton et al., "Ex vivo micro-computed tomography analysis of bleomycin-induced lung fibrosis for preclinical drug evaluation," Eur. Respir. J. **42**(6), 1633–1645, European Respiratory Society (2013) [doi:10.1183/09031936.00182412].

[4] E. D. Langhe et al., "Quantification of Lung Fibrosis and Emphysema in Mice Using Automated Micro-Computed Tomography," PLOS ONE **7**(8), e43123, Public Library of Science (2012) [doi:10.1371/journal.pone.0043123].

[5] D. J. Bartlett et al., "High-Resolution Chest Computed Tomography Imaging of the Lungs: Impact of 1024 Matrix Reconstruction and Photon-Counting Detector Computed Tomography," Invest. Radiol. **54**(3), 129–137 (2019) [doi:10.1097/RLI.0000000000000524].

[6] A. Inoue, "Impact of photon-counting CT on reader confidence in diagnosis of usual interstitial pneumonia," Oral, Chicago (2021).

[7] F. Pfeiffer et al., "Hard-X-ray dark-field imaging using a grating interferometer," 2, Nat. Mater. **7**(2), 134–137, Nature Publishing Group (2008) [doi:10.1038/nmat2096].

[8] F. G. Meinel et al., "Diagnosing and Mapping Pulmonary Emphysema on X-Ray Projection Images: Incremental Value of Grating-Based X-Ray Dark-Field Imaging," PLOS ONE **8**(3), e59526, Public Library of Science (2013) [doi:10.1371/journal.pone.0059526].

[9] F. G. Meinel et al., "Improved Diagnosis of Pulmonary Emphysema Using In Vivo Dark-Field Radiography," Invest. Radiol. **49**(10), 653–658 (2014) [doi:10.1097/RLI.0000000000000067].

[10] K. Hellbach et al., "In Vivo Dark-Field Radiography for Early Diagnosis and Staging of Pulmonary Emphysema," Invest. Radiol. **50**(7), 430–435 (2015) [doi:10.1097/RLI.0000000000000147].

[11] K. Hellbach et al., "X-Ray Dark-field Imaging to Depict Acute Lung Inflammation in Mice," Sci. Rep. **8**(1), 2096 (2018) [doi:10.1038/s41598-018-20193-8].

[12] R. Burkhardt et al., "Early detection of radiation-induced lung damage with X-ray dark-field radiography in mice," Eur. Radiol. **31**(6), 4175–4183 (2021) [doi:10.1007/s00330-020-07459-4].

[13] K. Scherer et al., "X-ray Dark-field Radiography - In-Vivo Diagnosis of Lung Cancer in Mice," Sci. Rep. **7**(1), 402 (2017) [doi:10.1038/s41598-017-00489-x].

[14] A. Yaroshenko et al., "Improved In vivo Assessment of Pulmonary Fibrosis in Mice using X-Ray Dark-Field Radiography," Sci. Rep. **5**, 17492 (2015) [doi:10.1038/srep17492].

[15] D. Attwood and A. Sakdinawat, "X-Rays and Extreme Ultraviolet Radiation: Principles and Applications," Cambridge Core, November 2016, [doi:10.1017/CBO9781107477629] (accessed 28 March 2021).

[16] T. Koenig et al., "On the origin and nature of the grating interferometric dark-field contrast obtained with low-brilliance x-ray sources," Phys. Med. Biol. **61**(9), 3427–3442 (2016) [doi:10.1088/0031-9155/61/9/3427].

[17] W. Yashiro, P. Vagovič, and A. Momose, "Effect of beam hardening on a visibility-contrast image obtained by X-ray grating interferometry," Opt. Express **23**(18), 23462–23471 (2015) [doi:10.1364/OE.23.023462].

[18] W. Yashiro, D. Noda, and K. Kajiwara, "Effect of insufficient temporal coherence on visibility contrast in X-ray grating interferometry," Opt. Express **26**(2), 1012–1027 (2018) [doi:10.1364/OE.26.001012].

[19] W. Yashiro and A. Momose, "Effects of unresolvable edges in grating-based X-ray differential phase imaging," Opt. Express **23**(7), 9233 (2015) [doi:10.1364/OE.23.009233].

[20] Y. Yang and X. Tang, "The second-order differential phase contrast and its retrieval for imaging with x-ray Talbot interferometry," Med. Phys. **39**(12), 7237–7253 (2012) [doi:10.1118/1.4764901].

[21] T. Köhler, K. J. Engel, and E. Roessl, "Noise properties of grating-based x-ray phase contrast computed tomography," Med. Phys. **38**(S1), S106–S116 (2011) [doi:https://doi.org/10.1118/1.3532396].

[22] F. De Marco et al., "Analysis and correction of bias induced by phase stepping jitter in grating-based X-ray phase-contrast imaging," Opt. Express **26**(10), 12707–12722 (2018) [doi:10.1364/OE.26.012707].

[23] V. Revol et al., "Noise analysis of grating-based x-ray differential phase contrast imaging," Rev. Sci. Instrum. **81**(7), 073709 (2010) [doi:10.1063/1.3465334].

[24] J. I. Sperl et al., "A Fourier-domain algorithm for total-variation regularized phase retrieval in differential X-ray phase contrast imaging," Opt. Express **22**(1), 450–462, Optical Society of America (2014) [doi:10.1364/OE.22.000450].

[25] T. Thüring et al., "Non-linear regularized phase retrieval for unidirectional X-ray differential phase contrast radiography," Opt. Express **19**(25), 25545–25558, Optical Society of America (2011) [doi:10.1364/OE.19.025545].

[26] W. Haas et al., "Phase-unwrapping of differential phase-contrast data using attenuation information," in Medical Imaging 2011: Image Processing **7962**, p. 79624R, International Society for Optics and Photonics (2011) [doi:10.1117/12.877945].

[27] F. M. Epple et al., "Unwrapping differential x-ray phase-contrast images through phase estimation from multiple energy data," Opt. Express **21**(24), 29101–29108, Optical Society of America (2013) [doi:10.1364/OE.21.029101].

[28] J. D. Armstrong et al., "Clinical evaluation of unsharp masking and slit scanning techniques in chest radiography.," Radiology **147**(2), 351–356, Radiological Society of North America (1983) [doi:10.1148/radiology.147.2.6340155].

[29] M. Bech, "X-ray imaging with a grating interferometer."

[30] C. J. Scotton and R. C. Chambers, "Bleomycin revisited: towards a more representative model of IPF?," Am. J. Physiol.-Lung Cell. Mol. Physiol. **299**(4), L439–L441, American Physiological Society (2010) [doi:10.1152/ajplung.00258.2010].

[31] D. M. Vasilescu et al., “Assessment of morphometry of pulmonary acini in mouse lungs by nondestructive imaging using multiscale microcomputed tomography,” Proc. Natl. Acad. Sci. **109**(42), 17105–17110, National Academy of Sciences (2012) [doi:10.1073/pnas.1215112109].

[32] D. Yu et al., “Comparison of the gas-liquid dual support fixation and Heitzman fixation techniques for preparing lung specimens,” Exp. Ther. Med. **14**(1), 825–830 (2017) [doi:10.3892/etm.2017.4563].

[33] C. C. W. Hsia et al., “An Official Research Policy Statement of the American Thoracic Society/European Respiratory Society: Standards for Quantitative Assessment of Lung Structure,” Am. J. Respir. Crit. Care Med. **181**(4), 394–418 (2010) [doi:10.1164/rccm.200809-1522ST].

[34] T. Weitkamp et al., “X-ray phase imaging with a grating interferometer,” Opt. Express **13**(16), 6296–6304 (2005) [doi:10.1364/opex.13.006296].

[35] A. Biguri et al., “TIGRE: a MATLAB-GPU toolbox for CBCT image reconstruction,” Biomed. Phys. Eng. Express **2**(5), 055010, IOP Publishing (2016) [doi:10.1088/2057-1976/2/5/055010].

[36] M. Ochs, “A brief update on lung stereology,” J. Microsc. **222**(3), 188–200 (2006) [doi:https://doi.org/10.1111/j.1365-2818.2006.01587.x].

[37] “Expert Automated Registration — 3D Slicer documentation,” <https://slicer.readthedocs.io/en/latest/user_guide/modules/expertautomatedregistration.html> (accessed 23 August 2021).

[38] “ImageJ,” <https://imagej.nih.gov/ij/> (accessed 12 January 2022).

[39] J. Kittler and J. Illingworth, “Minimum error thresholding,” Pattern Recognit. **19**(1), 41–47 (1986) [doi:10.1016/0031-3203(86)90030-0].

[40] J. M. Bland and D. G. Altman, “Measuring agreement in method comparison studies,” Stat. Methods Med. Res. **8**(2), 135–160 (1999) [doi:10.1177/096228029900800204].

[41] A. Velroyen et al., “Grating-based X-ray Dark-field Computed Tomography of Living Mice,” EBioMedicine **2**(10), 1500–1506 (2015) [doi:10.1016/j.ebiom.2015.08.014].

[42] R. Burkhardt et al., “In-vivo X-ray dark-field computed tomography for the detection of radiation-induced lung damage in mice,” Phys. Imaging Radiat. Oncol. **20**, 11–16 (2021) [doi:10.1016/j.phro.2021.09.003].

[43] K. Hellbach et al., “Facilitated Diagnosis of Pneumothoraces in Newborn Mice Using X-ray Dark-Field Radiography,” Invest. Radiol. **51**(10), 597–601 (2016) [doi:10.1097/RLI.0000000000000285].

[44] V. Ludwig et al., “Exploration of different x-ray Talbot–Lau setups for dark-field lung imaging examined in a porcine lung,” 065013, IOP Publishing (2019) [doi:10.1088/1361-6560/ab051c].

[45] Z. Wang and M. Stampanoni, “Quantitative x-ray radiography using grating interferometry: a feasibility study,” Phys. Med. Biol. **58**(19), 6815–6826, IOP Publishing (2013) [doi:10.1088/0031-9155/58/19/6815].